



Activation of Oxygen Redox by Inhibited Dynamic Phase Transition for High-Energy Li-Rich Layered Oxide Cathode

Junseong Kim^{a,b,1}, Hobin Ahn^{a,b,1}, Jinho Ahn^{a,b}, Hyunyoung Park^{a,b}, Jihyun Hong^c, Myeong Hwan Lee^{a,d}, Hyeokjun Park^{e,*}, Jongsoo Kim^{a,b,d,*}

^a Department of Energy Science, Sungkyunkwan University, Suwon 16419, Republic of Korea

^b SKKU Institute of Energy Science and Technology, Sungkyunkwan University, Suwon 16419, Republic of Korea

^c Energy Materials Research Center, Korea Institute of Science and Technology (KIST), 14 Gil 5, Hwarang-ro, Seongbuk-gu, Seoul 02792, Republic of Korea

^d Advanced Energy Materials Research Center, Korea Research Institute of Chemical Technology (KRICT), 141, Gajeongro, Yuseong, Daejeon 34114, Republic of Korea

^e Interdisciplinary Materials Measurement Institute, Korea Research Institute of Standards and Science (KRISS), 267, Gajeongro, Yuseong-gu, Daejeon, 34113, Republic of Korea

ARTICLE INFO

Keywords:

Li-ion batteries
Li-rich cathode material
Anion redox reaction
Phase transition
First-principles calculation

ABSTRACT

Li-rich layered oxides have garnered tremendous research interest as a promising high-energy cathode by harnessing combined cationic and anionic redox. Despite the great promise of oxygen redox, however, the distinct activity of oxygen redox in Li-rich materials has inhibited the precise understanding of the oxygen redox activation mechanism. Herein, we unravel the interplay between de/activation of oxygen redox and the phase transition behaviors of Li-rich cathodes through a comprehensive investigation of two Ru-based model Li-rich layered oxides, $\text{Li}_{1.2}\text{Ni}_{0.2}\text{Mn}_{0.3}\text{Ru}_{0.3}\text{O}_2$ and $\text{Li}_{1.2}\text{Ni}_{0.2}\text{Ru}_{0.6}\text{O}_2$. It is corroborated by synchrotron-based X-ray absorption spectroscopy analyses that the reversible oxygen redox occurs in $\text{Li}_{1.2}\text{Ni}_{0.2}\text{Mn}_{0.3}\text{Ru}_{0.3}\text{O}_2$ but the reaction is not triggered in $\text{Li}_{1.2}\text{Ni}_{0.2}\text{Ru}_{0.6}\text{O}_2$ despite high relevance in structure and stoichiometry. *Operando* X-ray diffraction elucidates that the O3-type $\text{Li}_{1.2}\text{Ni}_{0.2}\text{Ru}_{0.6}\text{O}_2$ undergoes a phase transition into the T3-type phase during charging while there is negligible structural change in O3-type $\text{Li}_{1.2}\text{Ni}_{0.2}\text{Mn}_{0.3}\text{Ru}_{0.3}\text{O}_2$. First-principles studies reveal that the theoretical redox potential to extract Li^+ from T3-type phase is significantly higher than that of O3-type $\text{Li}_{1.2}\text{Ni}_{0.2}\text{Ru}_{0.6}\text{O}_2$, inhibiting the activation of the oxygen redox. Our findings indicate the significance of the dynamic structural evolution on governing the activation of oxygen redox, thereby offering guidance for further design of Li-rich layered oxides toward the full utilization of the oxygen redox.

1. Introduction

With great advances made in the battery technology over the last few decades, it has become the most essential component of electrified portable devices and personal mobility [1]. As lithium-ion batteries (LIBs) are being intensively employed in an increasing number of large-scale applications, including electric vehicles and energy storage systems, the need for cathode materials particularly with higher energy density has become paramount. Despite successful adoptions of conventional cathode materials such as $\text{LiNi}_x\text{Co}_y\text{Mn}_{1-x-y}\text{O}_2$ (NCM), LiCoO_2 (LCO), and LiFePO_4 (LFP) in current state-of-the-art LIBs, however, their capacities are inherently limited by the charge compensation capability of transition metal (TM) redox centers [2–5]. Various energy storage

mechanisms have thus been explored to surpass the theoretical specific capacity of conventional cathode materials that merely rely on the TM redox. Anionic redox from lattice oxygen has been suggested as an extra charge storage mechanism that can be incorporated into conventional cathode systems. The cathode materials formulated with excessive lithium, so called lithium-rich layered oxide (LRLO, $\text{Li}_{1+x}(\text{TM})_{1-x}\text{O}_2$), are proven as an emerging class of high-energy cathode ($\sim 300 \text{ mAh g}^{-1}$) that can utilize more Li^+ owing to the cumulative cationic and anionic redox reactions [6–11].

The mechanistic understanding on the oxygen redox in LRLO has been a central topic, spurring extensive explorations of various LRLO types of cathodes, each of which exhibits unique electrochemical properties [9,12]. LRLO possesses a typical structural characteristic of

* Corresponding authors.

E-mail addresses: hjpark@kriss.re.kr (H. Park), jongsookim@skku.edu (J. Kim).

¹ These authors contributed equally to this work.

in-plane ordering (i.e. $\text{Li}_{1/3}\text{TM}_{2/3}$ honeycomb) induced by excessive Li^+ residing in TM layers, which offers a local bonding environment of A-O-Li (A: Na, Li, Va etc.). Theoretical calculations revealed that the local A-O-Li environment leads to the non-bonding state of O 2p orbitals which is the main participants for the oxygen redox reaction of LRLO cathodes [13–19]. Mn (3d) or Ru (4d)-based LRLO cathodes have been mainly subjected as promising LRLO cathodes as they can accommodate excessive Li^+ into structure owing to their high valence state and the feasibility of their oxygen redox activity was demonstrated by several experimental evidence [7,20–23]. In particular, Ru-based LRLO systems promise a good reversibility of oxygen redox likely due to the strong Ru (4d) – O (2p) hybridization, stimulating intensive studies on derivatives of Ru-based LRLO cathodes with diverse combinations of TM elements [12,24,25]. However, it has been reported that the activation of oxygen redox in Ru-based LRLO cathodes significantly differs depending on the TM compositions. For example, $\text{Li}_{1.2}\text{Ni}_{0.2}\text{Ru}_{0.6}\text{O}_2$ exhibits only cationic redox reactions of $\text{Ni}^{2+/4+}$ and $\text{Ru}^{4+/5+}$ without the participation of oxygen redox, while a successive cationic and anionic redox was proved with the nice electrochemical properties of the $\text{Li}_{1.2}\text{Co}_{0.4}\text{Ru}_{0.4}\text{O}_2$ cathode [26,27]. Though the degree of hybridization between TM and O orbitals was suggested to bring out such complex anionic oxygen redox activity depending on TM elements, a fundamental understanding on the role of TM composition on governing the activity of oxygen-redox chemistry in the LRLO system has still remained elusive to date [12]. Considering the crucial impacts of crystal structure on the oxygen-redox property of LRLO, resolving dynamic structural evolutions of LRLO cathodes during delithiation/lithiation might hold the key to elucidate the explicit influences of TM elements on oxygen-redox activation.

In this work, we investigate the electrochemical behaviors of two different Ru-based LRLO cathodes of $\text{Li}_{1.2}\text{Ni}_{0.2}\text{Mn}_{0.3}\text{Ru}_{0.3}\text{O}_2$ (LNMRO) and $\text{Li}_{1.2}\text{Ni}_{0.2}\text{Ru}_{0.6}\text{O}_2$ (LNRO) to uncover the interplay between the type of TM elements and oxygen redox activity. Despite the fact that both materials share analogous crystal structures and still have lithium contents in the structure after full oxidation to Ni^{4+} , Ru^{5+} and Mn^{4+} , it is found out that the LNMRO cathodes are able to deliver almost full utilization of Li^+ ($\sim 315.7 \text{ mAh g}^{-1}$) by implementing both cationic ($\text{Ni}^{2+/4+}$ and $\text{Ru}^{4+/5+}$) and anionic ($\text{O}^{2-/n-}$, $n < 2$) redox, while the LNRO cathodes only exhibit cationic redox corresponding to 232.9 mAh g^{-1} . The operando X-ray diffraction (XRD) studies unveil that LNMRO relatively well preserves its original structure without notable phase change throughout the whole electrochemical process, which is clearly distinct from the case of LNRO cathodes that undergo a substantial phase transition from O3-type to T3-type phase upon 3.8 V. The formation of the T3-type phase, by which Li ions occupy the tetrahedral site between TMO_6 octahedron and the LiO_6 octahedron, might hinder the activation of oxygen redox in LNRO during charging [28–30]. First-principles calculation results elaborate that the theoretical redox potential to extract Li^+ from LNRO significantly rises after the formation of the T3-type phase compared to the O3-type phase, indicating that further deintercalation of Li^+ via an oxygen redox reaction is nearly impossible. Electrochemical properties are also comparatively assessed for the cathodes, both showing reasonably stable but dissimilar responses depending on the presence of oxygen redox during cycling. These findings provide a new perspective on the structural interplay governing the de/activation of anionic oxygen redox reactions in Li-rich cathode materials.

2. Methods

2.1. Material preparation

Conventional solid-state synthesis method was employed to prepare the materials. Li_2CO_3 (Alfa Aesar, 99 %), MnCO_3 (Alfa Aesar, 99.9 %), $\text{Ni}(\text{OH})_2$ (Alfa Aesar, 96.34 %), and RuO_2 (Sigma Aldrich, 99.9 %) were used as precursors. The precursors were mixed in a stoichiometric amounts and subjected to high-energy ball milling at 400 rpm for 12 h in

an Ar-filled jar. Note that 5 % of excess Li_2CO_3 was more added to compensate for the volatilization of Li in high temperatures. Subsequently, the resulting powder was compressed into pellets and calcined in a quartz tube under a flow of dried air gas at 0.3 L min^{-1} . Calcination was carried out at $850 \text{ }^\circ\text{C}$ for 5 h.

2.2. Material characterization

The crystal structures of LNMRO and LNRO were analyzed using X-ray diffractometer (PANalytical Empyrean) with Mo $\text{K}\alpha$ radiation ($\lambda = 0.790319 \text{ \AA}$) in 2θ range of 5.01° to 34.99° with step size of 0.015° . For comparison with other studies, the 2θ angles of XRD pattern were converted to Cu $\text{K}\alpha$ radiation ($\lambda = 1.54178 \text{ \AA}$). Rietveld refinement was carried out using FullProf software. In operando XRD patterns were obtained during electrochemical operation at a current density of C/20 within the voltage range of 2.0–4.4 V. *Ex-situ* XRD patterns were obtained using pristine electrodes and electrodes that were fully discharged to 2.0 V after 20 and 50 cycles.

The atomic ratio of Li, Ni, Mn, and Ru in LNMRO and LNRO was determined using inductively coupled plasma atomic emission spectroscopy (ICP-AES; OPTIMA 8300, Perkin-Elmer) at the National Center for Inter-University Research Facilities (NCIRF) at Seoul National University.

Field-emission scanning electron microscopy (FE-SEM; Gemini SEM 560, ZEISS) was used to investigate the particle morphology and particle size of LNMRO and LNRO at the National Center for Inter-University Research Facilities (NCIRF) at Seoul National University.

High-resolution transmission electron microscopy (HR-TEM) image, transmission electron microscopy-energy dispersive X-ray spectroscopy (TEM-EDS) mapping images, and selected area electron diffraction (SAED) patterns were acquired using field-emission transmission electron microscopy (FE-TEM; JEM-F200, JEOL Ltd.) at Seoul National University's National Center for Inter-University Research Facilities (NCIRF). Each information was recorded using a $4\text{k} \times 4\text{k}$ CCD camera.

Ex-situ X-ray absorption spectroscopy (XAS) spectra for the Ru, Ni, and Mn K-edge were obtained at the 6D UNIST-PAL beamline at Pohang Accelerator Laboratory (PAL). Ru, Ni, and Mn K-edge spectra were collected in transmission mode with energy ranges of 21917–23088, 8133–9191, and 6339–7397 eV, respectively. Reference spectra were simultaneously obtained by using Ru, Ni, and Mn metal foil. Soft X-ray absorption spectroscopy (sXAS) spectra for the O K-edge were measured in high-energy grating (HEG) with a photon energy range of 525–560 eV at the 4D PES beamline at PAL. The collected XAS and sXAS data were analyzed using Athena software [31]. Each sample was prepared in the form of an electrode.

X-ray photoelectron spectroscopy (XPS) measurements were performed using an AXIS SUPRA (Kratos Analytical) at Seoul National University's National Center for Inter-University Research Facilities (NCIRF) to confirm the oxygen redox reaction. XPSPEAK41 software was used for XPS fitting after all data were calibrated at the binding energy of 284.6 eV for the C 1 s peak.

2.3. Electrochemical characterization

To make the LNMRO and LNRO electrodes, 70 wt% active material, 20 wt% Super P carbon black, and 10 wt% polyvinylidene fluoride (PVDF) was mixed using N-methyl-2-pyrrolidone (NMP) as a solvent. The mixture was cast on aluminum foil with a thickness of 200 μm and dried overnight at $100 \text{ }^\circ\text{C}$ under vacuum conditions. The electrode was then punched into a disk of 10 mm diameter, with a mass loading of $\sim 2 \text{ mg cm}^{-2}$. CR2032-type coin cells as a half-cell were assembled with Li metal as a counter electrode, a separator (Celgard 2400), and 1.2 M LiPF₆ in ethylene carbonate (EC): dimethyl carbonate (DMC) = 3:7 v/v as the electrolyte in an Ar-filled glove box. Galvanostatic charge/discharge tests were conducted at different current densities from C/20 to 2C rate within a voltage range of 2.0–4.4 V (vs Li^+/Li). The current

density of 1C rate was set to be 325.3 mA g⁻¹ and 285.4 mA g⁻¹ for LNMRO and LNRO, respectively. The charge current density was fixed at C/20, and tests were performed using an automatic battery charge/discharge test system (WBCS 3000, WonATech). The cyclic voltammetry (CV) test was conducted in the voltage range of 2.0–4.4 V at a scan rate of 0.5 mV s⁻¹ for the initial charge/discharge process. Galvanostatic intermittent titration technique (GITT) analyses of the electrodes were performed at a current density of C/20 with 60 min of charge/discharge and 30 min of rest for each step. The cycle performance was evaluated at a current density of C/5 during 50 cycles.

2.4. Computational details

All the DFT calculations were conducted by the ab initio Simulation Package (VASP). Projector-augmented wave (PAW) pseudopotentials were used with a plane-wave basis set, as implemented in VASP [32]. Perdew-Burke-Ernzerhof (PBE) parameterization of the generalized gradient approximation (GGA) was adopted for the exchange–correlation functional [33]. A 6×3×3 k-point grid was used to calculate the structures of Li_{1.4}Ni₃Mn₄Ru₃O₂₄ and Li_{1.4}Ni₃Ru₇O₂₄. The GGA+U method was adopted to address the localization of the d-orbitals in Ni, Mn, and Ru ions, with a value of 6.0, 3.9, and 4.0, respectively, as validated in previous reports [34–36]. The Heyd-Scuseria-Ernzerhof (HSE06) hybrid functional was applied to accurately calculate the projected density of states (pDOS) of Ni, Mn, Ru, and O [37]. The kinetic-energy cutoff of 500 eV was selected in all the calculations and all the structures were optimized until the unit cell force converged to within 0.03 eV Å⁻¹. Schematic figures and the crystal structures were depicted using VESTA software [38].

From the obtained structural information from XRD and Rietveld refinement analysis, cluster-assisted statistical mechanics (CASM) software was utilized to gain the various Li-deficient phases of Li_xNi_{0.2}Mn_{0.3}Ru_{0.3}O₂ and Li_xNi_{0.2}Ru_{0.6}O₂ (0 ≤ x ≤ 1.2) [39,40]. Direct first-principles calculations were conducted on a maximum of 20Li⁺/vacancy configurations with low electrostatic energies acquired by Ewald summation at each delithiated phase. Calculated formation energies were arranged in a form of convex-hull plot to compare the thermodynamic stability of Li_xNi_{0.2}Mn_{0.3}Ru_{0.3}O₂ and Li_xNi_{0.2}Ru_{0.6}O₂. The theoretical redox potentials of Li_xNi_{0.2}Mn_{0.3}Ru_{0.3}O₂ and Li_xNi_{0.2}Ru_{0.6}O₂ were estimated by the following equations:

$$V = -\frac{E[\text{Li}_{x_2}\text{Ni}_{0.2}\text{Mn}_{0.3}\text{Ru}_{0.3}\text{O}_2] - E[\text{Li}_{x_1}\text{Ni}_{0.2}\text{Mn}_{0.3}\text{Ru}_{0.3}\text{O}_2] - (x_2 - x_1)E[\text{Li}]}{(x_2 - x_1)F} \quad (1)$$

$$V = -\frac{E[\text{Li}_{x_2}\text{Ni}_{0.2}\text{Ru}_{0.6}\text{O}_2] - E[\text{Li}_{x_1}\text{Ni}_{0.2}\text{Ru}_{0.6}\text{O}_2] - (x_2 - x_1)E[\text{Li}]}{(x_2 - x_1)F} \quad (2)$$

where V is the average redox potential in the range of x₁ ≤ x ≤ x₂; E stands for the lowest formation energy at each configuration of Li_xNi_{0.2}Mn_{0.3}Ru_{0.3}O₂ and Li_xNi_{0.2}Ru_{0.6}O₂ compositions; F and E[Li] are the Faraday constant and Li metal energy, respectively.

3. Results and discussion

3.1. Structural characterization of LNMRO and LNRO

We designed two model Ru-based Li-rich layered oxide cathodes of Li_{1.2}Ni_{0.2}Mn_yRu_{0.6-y}O₂ (y = 0, LNRO and y = 0.3, LNMRO), which are iso-structural but only compositionally different by substituting some of Ru⁴⁺ to iso-valent Mn⁴⁺. Comparative investigations on two materials, which are known to exhibit significantly different electrochemical behaviors, enable to study the role of TM elements on determining the activity of oxygen anionic redox in Li-rich layered cathodes. The theoretical capacities of LNMRO and LNRO are 325.3 mAh/g and 285.4 mAh/g assuming all 1.2 mol of Li⁺ are extracted, respectively. It is also

notable that the cationic redox (i.e., Ni^{2+/4+} & Ru^{4+/5+}) can provide a charge capacity (189.8 mAh/g) corresponding to 0.7 mol of Li⁺ deintercalation in LNMRO, while LNRO can induce 1.0 mol of Li⁺ delithiation (237.8 mAh/g) by cationic charge compensations. We prepared LNMRO and LNRO powders via solid-state synthesis as described in experimental section. The formation of layered structure of LNMRO and LNRO was confirmed by the results of Rietveld refinements based on the X-ray diffraction patterns in Fig. 1a–b. The details of structural information including atomic positions and occupancies are tabulated in Table S1 and Table S2. In both materials, a clear superstructure of honeycomb-like ordering in the TM layer was manifested in the 2θ range of 20°–32°. The presence of typical superstructure patterns also verifies the excessive Li⁺ accommodation into the layered structure that resides on TM sites in TM layer [41,42]. Scanning electron microscopy analysis results in Fig. 1c–d present that the morphologies of the synthesized LNMRO and LNRO are similar to each other, and their particle sizes are around 100 ~ 400 nm. High resolution transmission electron microscopy (HR-TEM) images confirmed the single-crystallinity of layered-structure of two synthesized materials. In addition, the elemental mapping of LNMRO and LNRO by energy dispersive X-ray spectroscopy (EDS) revealed the homogeneous distribution of elements throughout the particles without local ingenuity (Fig. S1). Furthermore, the successful synthesis with targeted chemical composition of LNMRO and LNRO was confirmed by inductively coupled plasma atomic emission spectroscopy (ICP-AES) measurements (Table S3 and Table S4). The average oxidation states of Mn, Ni, and Ru were assessed by X-ray absorption nearest edge spectroscopy (XANES, Mn K-edge, Ni K-edge, Ru K-edge) analysis, which indicates that the as-prepared LNMRO and LNRO are composed of Ni²⁺, Ru⁴⁺ and Mn⁴⁺ (Fig. S2). Redox activity of two cathodes were investigated by CR2032-type coin Li half cells at C/20 within the voltage range of 2.0–4.4 V (vs. Li⁺/Li). The current densities of 1C for LNMRO and LNRO are 325.3 mA g⁻¹ and 285.4 mA g⁻¹, respectively, which is based on their theoretical capacities. Fig. 1e–f display the charge/discharge curves for initial cycle of LNMRO and LNRO, respectively. LNMRO could deliver a high charge capacity of ~ 315.7 mAh/g corresponding to ~ 1.16 mol Li⁺ deintercalation (utilizing ~ 97.0 % of theoretical capacity). The amount of Li⁺ extracted (~1.16 mol) over the capacity from cationic redox (0.7 mol) directly implies the participation of anionic redox from the lattice oxygen in LNMRO. However, it is verified that the charge capacity of LNRO is ~ 232.93 mAh/g under the same testing condition. The obtained capacity accounts for the ~ 0.98 mol of Li⁺ extraction, which almost matches the amount of electrons from the cationic redox reactions of Ru^{4+/5+} and Ni^{2+/4+}, inferring the non-activity of oxygen redox in LNRO system. It is also noteworthy that the LNMRO exhibit a typical staircase plateau behavior with the activation of oxygen redox while a slanted voltage profile is observed for LNRO. This dissimilar oxygen redox behavior despite the same crystal structure makes it meaningful to re-examine the mechanistic differences between two Li-rich cathode materials, the detail of which will be discussed in the followings.

3.2. Redox-reaction mechanism of LNMRO and LNRO

To clarify the charge storage mechanism of LNMRO and LNRO, ex-situ XANES analyses were conducted for samples with different states of charge to track the oxidation state changes of each element. The white line of Ru K-edge XANES spectrum of LNMRO shifted to higher energy level during charge up to 4.2 V (vs. Li⁺/Li) and then showed negligible variation during further delithiation to 4.4 V (a typical cut-off voltage for TM redox) in Fig. 2a. Analogous oxidation behaviors were also figured out in Ni K-edge XANES as shown in Fig. 2b, where a prominent shift to higher energy of Ni white line occurs up to 4.2 V followed by negligible changes upon 4.4 V. These results clearly indicate that the sequential redox reaction by TM (Ru^{4+/5+} & Ni^{2+/4+}) up to 4.2 V and then subsequent oxidation by lattice oxygen, the evidence of which will be further elaborated. By contrast, the Ru K-edge spectrum of LNRO

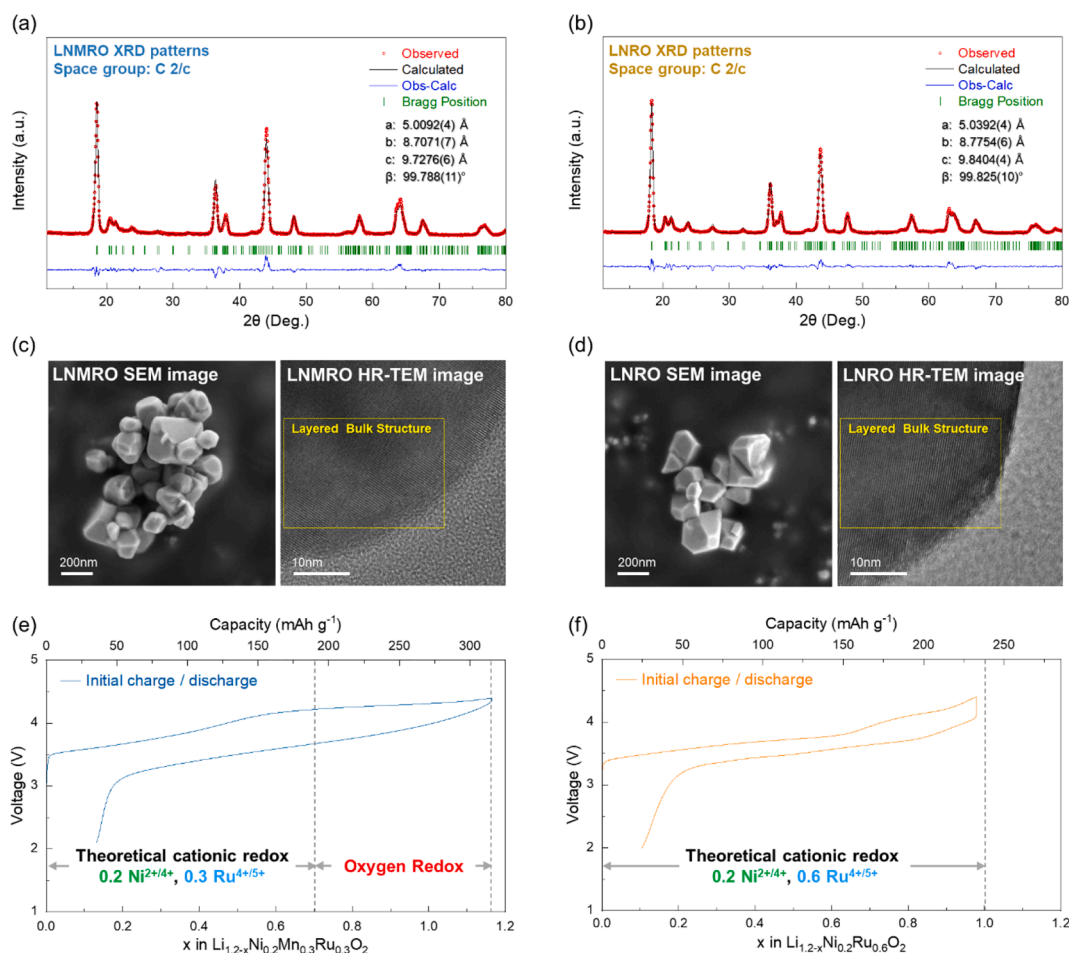


Fig. 1. Materials characterizations of LNMRO and LNRO: Rietveld refinement results of XRD patterns of (a) LNMRO and (b) LNRO. SEM and HR-TEM images of (c) LNMRO and (d) LNRO. Voltage profiles of (e) LNMRO and (f) LNRO for the first cycle at the current density of $C/20$ in the voltage range of 2.0–4.4 V.

shows a continuous shift to higher energy level during the entire charge reaction to 4.4 V (Fig. 2d), implying the distinct charge storage behaviors of LNRO. In the case of Ni K-edge spectra of LNRO, a significant peak shift was observed mostly during charging over 4.2 V to 4.4 V (Fig. 2e). The dynamic oxidation state change at the high voltage region likely suggests that most of the charge compensation is attributed to the Ru and Ni cations in LNRO system with no or less redox activity from O anion. Note that the oxidation state of Mn^{4+} is almost invariable during the entire charge/discharge process as shown in Fig. S3 despite involving the minimal alteration of Mn K-edge spectra due to distortion of MnO₆ polyhedron after the oxygen redox reaction [43]. In addition, soft X-ray absorption spectroscopy (sXAS) O K-edge spectra with various states of charge was presented to directly evidence the occurrence of the oxygen redox reaction of LNMRO and LNRO in Fig. 2c and Fig. 2f. It is referable that the increase in intensity of the e_g orbitals near at 530.4 eV indicates the oxidation of localized oxygen orbitals, thereby proving oxygen redox reaction [9,14,15,44–46]. We figured out that there was a pronounced difference in the peak intensity between 4.2 V and 4.4 V at 530.4 eV in LNMRO (Fig. 2c), demonstrating the oxygen redox activity in the upper voltage region [6,15,16,27,44,47]. On the other hand, the intensity variation at 530.4 eV was almost absent in LNRO during entire charging and discharging process (Fig. 2f). Together with XANES analysis results, these findings firmly elucidate the inhibition of the oxygen redox reaction in LNRO system unlike the case of LNMRO. Furthermore, ex situ X-ray photoelectron spectroscopy (XPS) analysis results of O 1s spectra also supported the reversible oxygen redox in LNMRO by showing appearance and disappearance of the peroxo-species in the charged/discharged state (Fig. S4) [48,49]. Density

functional theory (DFT) calculations were also carried out to elaborate the redox mechanisms of LNMRO and LNRO. Fig. 2g–h and Fig. S5 depict the projected density of states (pDOS) of Ru, Mn, Ni, and O atoms in $Li_xNi_{0.2}Mn_{0.3}Ru_{0.3}O_2$ (Li_x NMRO) and $Li_yNi_{0.2}Ru_{0.6}O_2$ (Li_y LNRO) and the visualized electron and hole densities in $Li_{0.417}$ NMRO and Li_0 NMRO, respectively. The sequential TM redox was confirmed by pDOS difference of Ru 4d between $Li_{1.2}$ NMRO and $Li_{0.917}$ NMRO, and Ni 3d between $Li_{0.917}$ NMRO and $Li_{0.417}$ NMRO, respectively (Fig. 2g). Then, the finding that dominant electron densities in O 2p orbitals below Fermi level in $Li_{0.417}$ NMRO are converted to the hole densities in Li_0 NMRO also explicates the oxidation of lattice oxygen at a high delithiated state (Fig. 2h). Contrary to the LNMRO, however, a distinct pDOS change was observed in LNRO where the oxidations of Ru and Ni cations are broadly found in various state of charge in LNRO (Fig. S5). The electron densities of Ru 4d–O 2p hybridized states in $Li_{1.2}$ NRO transformed into the hole densities in $Li_{0.583}$ NRO. During further delithiation to $Li_{0.083}$ NRO, particularly, the electron density of Ni 3d orbital was just changed to the hole density and there was negligible oxidation of the O anion. These combined experimental and theoretical results unequivocally corroborate the different activation behavior of the oxygen redox in the two materials: the lattice oxygen takes participation in charge compensation of LNMRO after full utilization of TM redox whereas LNRO is not capable of triggering the oxygen redox.

3.3. Relationship between structural evolution and oxygen redox activity of LNMRO and LNRO

We scrutinized the structural change during the initial charge/

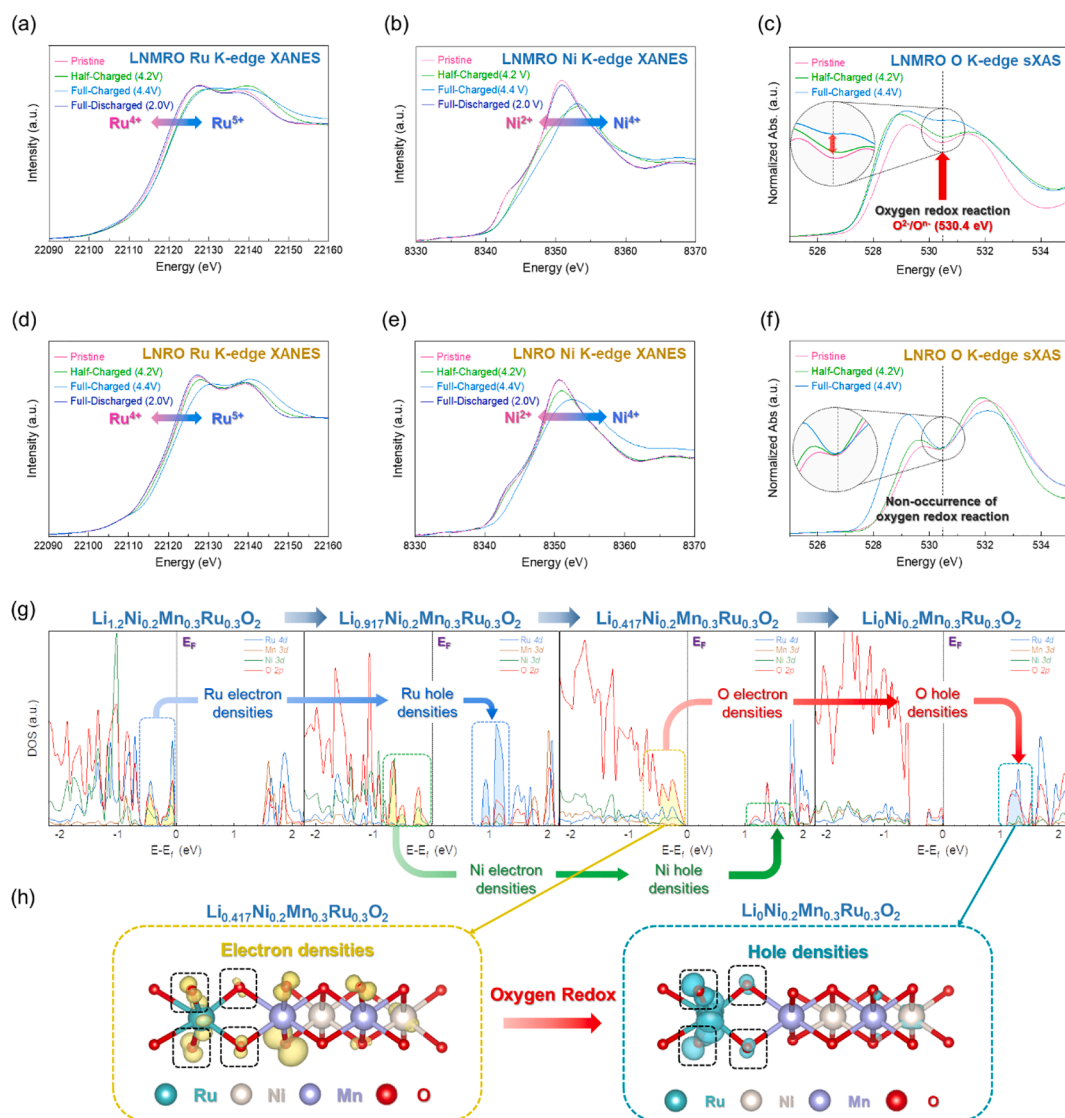


Fig. 2. Synchrotron-based XAS analysis of LNMRO and LNRO at different state of charge and first-principles calculation results of projected density of states (pDOS) and visualized charge density: Ex-situ XAS spectra at various states of LNMRO (a) Ru K-edge, (b) Ni K-edge, and (c) O K-edge. Ex-situ XAS spectra at various states of LNRO (d) Ru K-edge, (e) Ni K-edge, and (f) O K-edge. (g) pDOS of Ru, Ni, Mn and O atoms in various delithiated states of LNMRO. (h) Corresponding electron and hole densities in Li_{0.417}NMRO and Li₀NMRO, respectively.

discharge process of LNMRO and LNRO by using in operando X-ray diffraction (XRD) measurements to understand distinct redox mechanisms in the structural point of view. Fig. 3a describes that LNMRO shows a negligible shift of XRD patterns including main layered peak of (002) throughout the electrochemical cycling, indicating that the overall structures well maintained, except for the disappearance of superstructure patterns in the 2θ range of 20° - 25° . The point at which the superstructure pattern starts to diminish corresponds to the onset of the oxygen redox reaction, which means TM migration is happening in oxygen redox-based materials [50]. In stark contrast, the collected XRD patterns of LNRO in Fig. 3b exhibited markedly different behavior involving substantial structural changes. The XRD pattern of the LNRO was relatively unchanged until charged to 3.8 V. During the subsequent charging process, however, the intensity of the (002) peak tends to decrease, and an additional peak appears at a higher diffraction angle of $2\theta \approx 19^\circ$, manifesting a phase transition. The newly evolved phase above 3.8 V could be assigned to the T3-type phase of LNRO where the unit cell with contracted c-axis by Li⁺ occupying tetrahedral sites is reflected in the high-angle shifted (002) peak [51,52]. The reversed T3-O3 phase transition was also found during the subsequent discharge

process, confirming the reversibility of the phase transition in LNRO. More important is that the sharp superstructure patterns of LNRO were conserved throughout the entire electrochemical cycle, indicating the absence of TM migration and the mitigation of oxygen redox activity. The appearance of the T3-type phase at the upper voltage region implies that the suppressed activity of oxygen redox in LNRO might be strongly relevant to the structural characteristics of the T3-type phase. It is our rationale that the redox potential is increased to extract Li⁺ trapped in the tetrahedral site in the T3-type LNRO structure, resulting in the deactivation of the oxygen redox reaction in the voltage window up to 4.4 V. We also performed first-principles calculations to unveil the relationship between phase transition and TM migration behaviors of LNMRO and LNRO cathodes. The probability of the O3-T3 phase transition was evaluated through a comparison of formation energies of various Li-deficient phases of Li_xNMRO and Li_yNRO ($0 \leq x, y \leq 1.2$). Fig. 3c describes the convex-hull plot of Li_xNMRO where the O3-type phase is the most stable phase throughout all compositions, revealing the absence of a phase transition into the T3-type phase. However, the formation energy of a T3-type Li_{0.083}NRO was estimated as -78.48 meV f.u.⁻¹, which becomes lower than that of the O3-type Li_{0.083}NRO

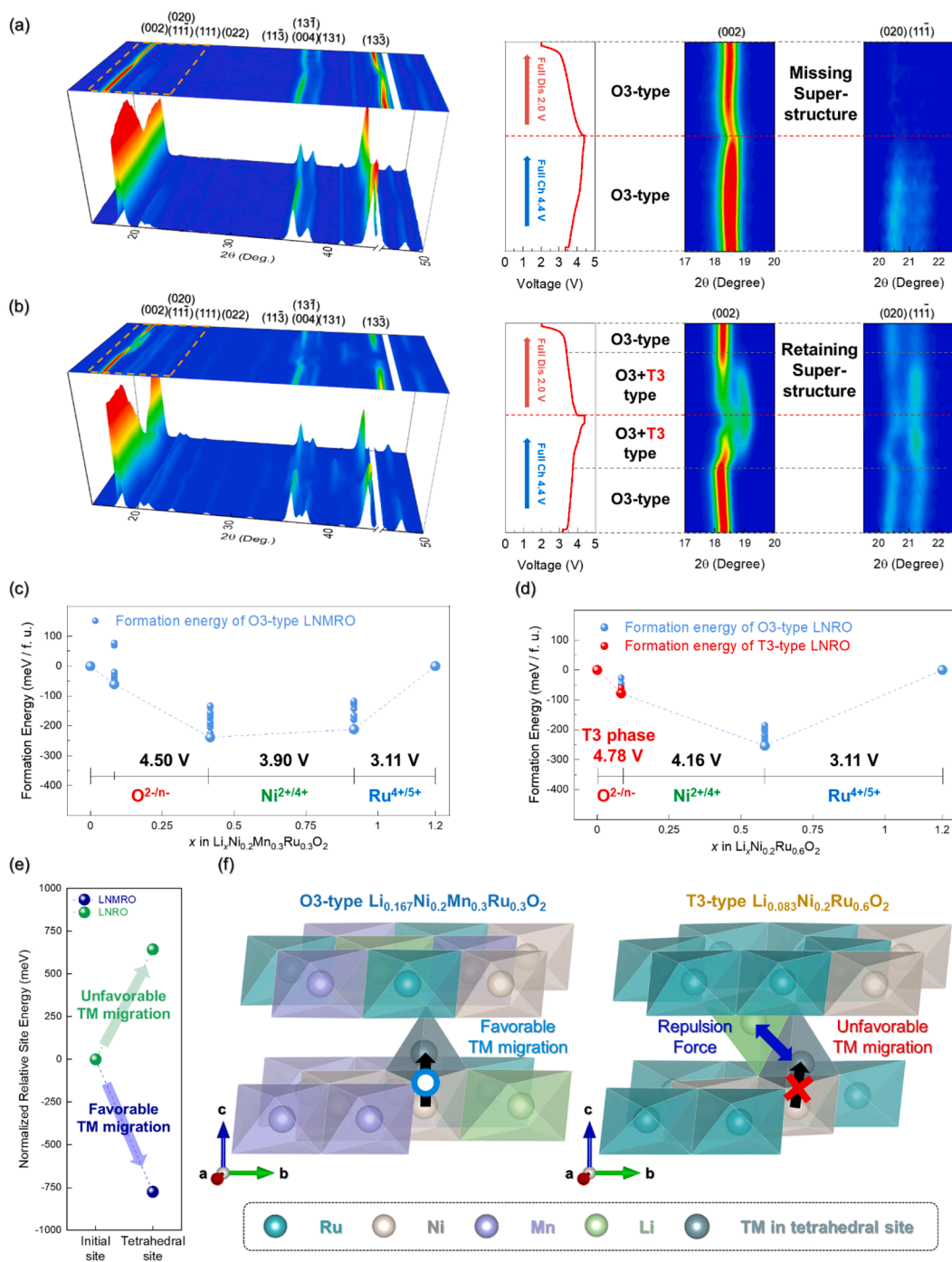


Fig. 3. Operando XRD analysis and first-principles calculation results: Contour maps of *in situ* XRD patterns of (a) LNMRO and (b) LNRO recorded during initial cycle in the voltage range of 2.0–4.4 V. Magnified view of 2θ ranges for (002) peak and superstructure. Formation energies and corresponding voltage prediction results of (c) LNMRO and (d) LNRO. (e) Calculated relative energy of TM in octahedral and tetrahedral sites. (f) Schematic illustrations on the TM migration.

(−69.48 meV f.u.^{−1}) at a highly delithiated state as shown in Fig. 3d. It means that the O3-T3 phase transition is energetically favorable in LNRO at a high state of charge (SoC) after the cationic redox reactions. We expect that the relatively large amounts of high-valent Ru⁵⁺ at the highly delithiated phase of LNRO, whose Ru content is twice that of LNMRO, experience electrostatic repulsion with Li⁺ located at the tetrahedral sites in the Li-layer. It is reasonable that Li⁺ occupying the tetrahedral site could not further migrate into the neighboring octahedral site in the Li-layer due to the strong repulsion by TM cations in the TM-layer. The trapped Li⁺ in tetrahedral sites results in the structural transition of LNRO into the T3-type phase. More importantly, the O3-T3

phase transition in LNRO results in an increase of the theoretical redox potential required for further delithiation from Li_{0.083}NRO (4.67 V → 4.78 V). The relatively high redox potential of Ni cation in LNRO compared to the case of LNMRO observed in Fig. 3d is also attributed to the structural transition of LNRO into the T3-type phase during charge. It is analogous to the higher redox potential of Ni^{2+/4+} in spinel-type LiNi_{0.5}Mn_{1.5}O₄ cathodes (> ~4 V), where Li⁺ is extracted from tetrahedral sites, than conventional NCM type cathodes with Li⁺ extraction from octahedral sites [53,54]. Accordingly, the further delithiation accompanied by oxygen redox in the T3-type LNRO is suppressed in the voltage range of 1.5–4.4 V probably due to the trapped Li⁺ in the

tetrahedral site. The energetics of TM migration were also examined to gain further insights on the structural impacts on oxygen redox in LNMRO and LNRO. It should be noted that TM-migration behaviors are strongly correlated with the occurrence of oxygen redox to stabilize the oxidized oxygen ions [44,55]. Fig. 3e presents the normalized relative site energy of TM between the original octahedral site and the migrated neighboring tetrahedral site in the Li-layer which shares faces with the original position. TM-migration into the tetrahedral site is an energetically downhill process in LNMRO likely accompanying the oxygen redox reactions, as evidenced in previous sections. However, TM-migration in LNRO requires a high energy about 643.29 meV according to the calculated relative TM migration energy, indicating that the TM-migration in LNRO is thermodynamically difficult. This is probably due to the structural characteristics of the T3-type phase where Li^+

occupying the tetrahedral sites electrically repel TM ions to prevent the TM moving down into the Li-layer (Fig. 3f). These findings on the phase transition and TM-migration behaviors calculated from theory are well consistent with the experimental interpretations derived from the operando XRD measurements for LNMRO and LNRO. Furthermore, we also checked the structural change of the two materials after long-term cycling through *ex-situ* XRD analysis (Fig. S6). It is noticeable that the superstructure peaks of LNMRO diminished after 50 cycles and the (002) peak shifted to a significantly low angle, indicating the elongated *c*-lattice parameter accompanied by substantial TM migration because of oxygen redox. On the other hand, there was only a slight structural change of LNRO with relatively well conserved superstructure owing to the deactivation of oxygen redox by the O3-T3 phase transition, which is in good agreement with our operando XRD analysis results [56].

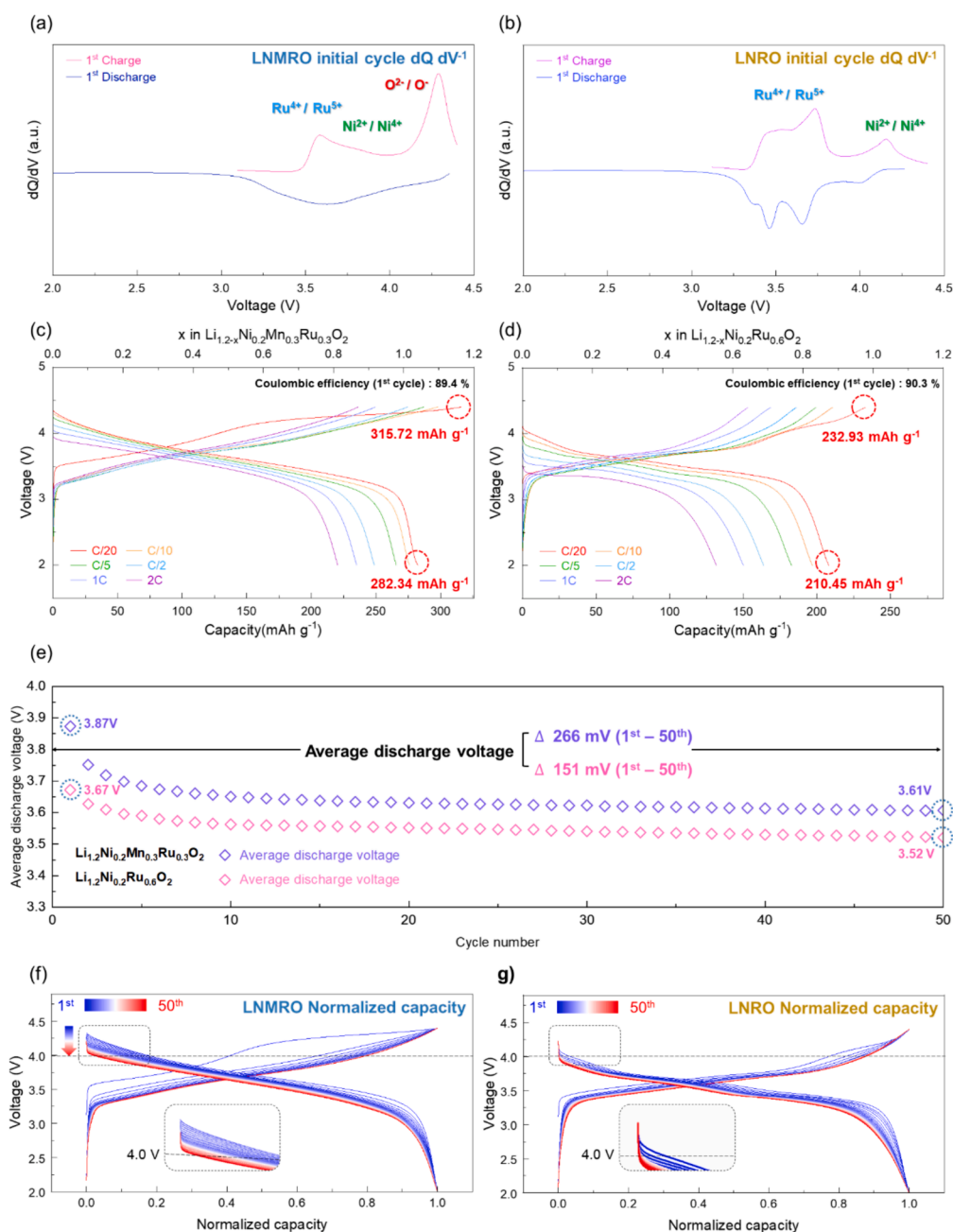


Fig. 4. Electrochemical properties of LNMRO and LNRO: Differential capacity versus voltage (dQ dV^{-1}) curves of (a) LNMRO and (b) LNRO for initial cycle. Charge/discharge curves of (c) LNMRO and (d) LNRO at different discharge current densities and charge current density of C/20. (e) Average discharge voltage of LNMRO and LNRO in the voltage range of 2.0–4.4 V at current density of 0.2C. Normalized charge/discharge curves for 50 cycles in (g) LNMRO and (h) LNRO.

3.4. Electrochemical properties of LNMRO and LNRO

Having confirmed the impact of structural transformation on the activation of the oxygen redox reaction, we investigated various electrochemical properties of LNMRO and LNRO cathodes in the voltage range of 2.0–4.4 V (vs Li⁺/Li). The differential curve (dQ dV⁻¹) of the galvanostatic charge/discharge profiles for LNMRO in Fig. 4a represents a typical dQ dV⁻¹ plot of Li-rich layered cathodes utilizing both cationic and anionic redox, showing that the broad peaks are assigned to the cationic redox (Ru^{4+/5+} and Ni^{2+/4+}) below 4.0 V and the sharp peak appearing around 4.25 V indicates an anionic redox reaction of O^{2-/n-} (n < 2) in the high voltage region. As shown in Fig. 4b, however, the dQ dV⁻¹ curve of LNRO exhibited that most of the redox reactions end up below the onset of the oxygen redox potential (~4.2 V) in LNMRO, with non-occurrence of anionic redox (O^{2-/n-}). Each peak at about 3.5 V and 4.2 V is ascribed to the redox reaction of Ru^{4+/5+} and Ni^{2+/4+}, respectively. Identical behaviors were also manifested in cyclic voltammetry (CV) investigations of the two materials (Fig. S7). The CV curve of LNMRO featured two apparent redox peaks attributed to cationic redox by Ni^{2+/4+} and Ru^{4+/5+} below 4.2 V followed by a strong peak corresponding to anionic oxygen oxidation. On the other hand, LNRO exhibited a broad redox peak in the CV curve throughout the entire voltage range during the charging process, indicating the absence of characteristic oxygen redox. The distinct oxygen redox activity of LNMRO and LNRO was again confirmed even at a higher charge cut-off condition applied (Fig. S8 and S9). It is understandable that Li⁺ extraction from the tetrahedral site in the spinel-like structure of the T3-type phase LNRO raised the oxidation potential of the Ni^{2+/4+} redox in LNRO higher than that of LNMRO, which is also in accordance with our experimental observations and theoretical models. Fig. S10 also shows the comparison of theoretically predicted redox potentials and initial charge/discharge curves of LNMRO and LNRO. The theoretical redox potentials were well matched with the experimentally measured charge/discharge profiles. The power capabilities of LNMRO and LNRO cathodes were also examined as shown in Fig. 4c-d, respectively. At C/20, LNMRO and LNRO delivered ~ 282.34 and ~ 210.45 mAh/g, respectively, which means a larger energy density of LNMRO than that of LNRO. Interestingly, whereas the capacity of LNRO at 2C was just retained up to 63.3 % of the capacity measured at C/20, LNMRO cathodes delivered a large specific capacity of ~ 220.3 mAh/g at 2C, which corresponds to ~ 78.0 % of the capacity measured at C/20. In addition, galvanostatic intermittent titration technique (GITT) measurements of LNMRO and LNRO were performed to compare the kinetic properties of the two cathodes. As shown in Fig. S11, LNMRO exhibited very little polarization across almost the whole range of voltage. However, LNRO showed a significant potential drop in the high voltage range, which might result from limited Li⁺ diffusion in T3-type LNRO cathodes. Considering the relatively sluggish kinetics of the oxygen redox in most of LRLOs, it is astonishing that LNMRO exhibited better power capability than LNRO even with exploiting the oxygen redox. We speculated that the different power capability between LNMRO and LNRO might come from their disparate phase transition behaviors. Li⁺ trapped in the tetrahedral site and contracted c-lattice in T3-type LNRO might hinder the diffusion of other Li⁺, while the relatively invariant structure of LNMRO is able to ensure facile Li⁺ transport during the electrochemical cycling. The power capability tests for repeated cycles in Fig. S12 also uphold our suggestion on the structural influences on kinetic properties of the LNMRO and LNRO. In addition, we compared the cycle performances of LNMRO and LNRO (Fig. S13). It was verified that LNMRO exhibit slightly poor cyclability than LNRO, which is attributed to both the occurrence of oxygen redox in only LNMRO and the larger contents of de/intercalated Li⁺ from the LNMRO structure compared to the LNRO structure. The higher capacity retention of LNRO might originate from the absence of oxygen redox, which is suppressed by the T3 phase transition that effectively interrupts TM migration and maintains the original crystal structure. In comparison of the cyclability between

LNRO and LNMRO, the interesting point is the variation of voltage profiles during prolonged cycling. It was reported that oxygen redox reaction results in the continuous voltage decay during prolonged cycling because of TM migration to the Li-layer [45]. The average discharge voltages of LNMRO and LNRO for 50 cycles were arranged in Fig. 4e. For the 50 cycles, LNMRO and LNRO exhibited the voltage reductions of 266 mV and 151 mV, respectively. The larger voltage decay in LNMRO compared to LNRO is due to the occurrence of the oxygen redox reaction. Moreover, as shown in Fig. 4f-g, LNRO relatively well maintained its original charge/discharge curves from 1st to 50th cycles, while LNMRO exhibited voltage decay especially in the high voltage range above 4 V during the same electrochemical cycles. Through the differential capacity versus voltage profiles (dQ dV⁻¹) on the cycle performances (Fig. S14), it was also verified that LNMRO with the oxygen redox reaction delivered relatively large voltage decay and remarkable changes in the charge/discharge profile compared to LNRO. These cyclability results clearly show the occurrence of oxygen redox in LNMRO, which is well matched with the various experimental and calculation results.

4. Conclusion

We successfully correlated the de/activation of oxygen redox to the redox potential modulation as a result of dynamic structural evolution through a comparative examination on two Ru-based model LRLO cathodes. Although the two materials possess an analogy in their crystal structure and stoichiometry, the activation of oxygen redox is possible for LNMRO cathodes whereas LNRO could not trigger the oxygen redox. At C/20, LNMRO delivered the charge capacity of ~ 315.7 mAh/g, corresponding to ~ 1.16 mol Li⁺ deintercalation through both the cationic Ni and Ru redox and the anionic oxygen redox. On the other hand, LNRO just exhibited ~ 232.93 mAh/g at the same conditions, corresponding to ~ 0.98 mol Li⁺ deintercalation through only cationic Ni and Ru redox. The ex-situ synchrotron-based XANES and sXAS results clearly indicated that both the TM-based cationic redox and the oxygen redox reaction are occurred in LNMRO, whereas LNRO only shows the redox reaction based on the TM cations without oxygen redox. It was also revealed from operando XRD analyses that LNMRO conserves the overall crystal structure even with the progressive oxygen redox except for the vanishing of super-lattice by the TM-migration. On the other hand, in the case of LNRO, the substantial O3-T3 phase transition happens during charge/discharge, which is also supported by first-principles calculation. The calculation results suggested the formation of T3-type phase significantly inhibits oxygen redox in LNRO by raising the theoretical voltage of further Li⁺ extraction from the T3-type phase beyond the operation voltage window. The distinct difference of electrochemical responses for LNMRO and LNRO depending on the oxygen redox were confirmed in the various testing conditions. It is noteworthy that LNRO show relatively poor power-capability, resulting from the sluggish Li⁺ diffusion induced by the highly decreased c-lattice parameter after O3-T3 phase transition. Specifically, the disparity in cycle performance between LNMRO and LNRO, including variations in the average operation voltage and charge/discharge profiles during cycling, further substantiates the presence of oxygen redox in LNMRO and its absence in LNRO. This work is the first to disclose the intricate relationship between the oxygen redox de/activation and structural characteristics in LRLO-type cathodes. We believe that this new mechanistic perspective will aid in the enrichment of rudimentary understanding of oxygen redox chemistry in various LRLO-type cathodes.

CRedit authorship contribution statement

Junseong Kim: Writing – original draft, Methodology, Formal analysis, Data curation. **Hobin Ahn:** Writing – original draft, Visualization, Validation, Formal analysis. **Jinho Ahn:** Visualization, Methodology, Investigation. **Hyunyoung Park:** Validation, Software, Data

curation. **Jihyun Hong**: Validation, Conceptualization. **Myeong Hwan Lee**: Validation, Methodology. **Hyeokjun Park**: Writing – review & editing, Supervision, Project administration, Data curation, Conceptualization. **Jongsoo Kim**: Writing – review & editing, Supervision, Resources, Project administration, Funding acquisition, Data curation, Conceptualization.

Declaration of competing interest

The authors declare that they have no known competing financial interests or personal relationships that could have appeared to influence the work reported in this paper.

Data availability

Data will be made available on request.

Acknowledgements

This research was supported National R&D Program through the National Research Foundation of Korea (NRF) funded by Ministry of Science and ICT (RS-2024-00408156) of Republic of Korea. In addition, the calculation resources were supported by the Supercomputing Center in Korea Institute of Science and Technology Information (KISTI) (KSC-2022-CRE-0415).

Appendix A. Supplementary data

Supplementary data to this article can be found online at <https://doi.org/10.1016/j.cej.2024.153122>.

References

- J.B. Goodenough, K.S. Park, The Li-ion rechargeable battery: A perspective, *J. Am. Chem. Soc.* 135 (2013) 1167–1176, <https://doi.org/10.1021/ja3091438>.
- H. Park, H. Park, K. Song, S.H. Song, S. Kang, K.-H. Ko, D. Eum, Y. Jeon, J. Kim, W. M. Seong, H. Kim, J. Park, K. Kang, In situ multiscale probing of the synthesis of a Ni-rich layered oxide cathode reveals reaction heterogeneity driven by competing kinetic pathways, *Nat. Chem.* 14 (2022) 614–622, <https://doi.org/10.1038/s41557-022-00915-2>.
- Y.-K. Sun, S.-T. Myung, B.-C. Park, J. Prakash, I. Belharouk, K. Amine, High-energy cathode material for long-life and safe lithium batteries, *Nat. Mater.* 8 (2009) 320–324, <https://doi.org/10.1038/nmat2418>.
- J.N. Zhang, Q. Li, C. Ouyang, X. Yu, M. Ge, X. Huang, E. Hu, C. Ma, S. Li, R. Xiao, W. Yang, Y. Chu, Y. Liu, H. Yu, X.Q. Yang, X. Huang, L. Chen, H. Li, Trace doping of multiple elements enables stable battery cycling of LiCoO₂ at 4.6 V, *Nat. Energy.* 4 (2019) 594–603, <https://doi.org/10.1038/s41560-019-0409-z>.
- A.K. Padhi, J.B. Goodenough, 12. S. Picart and E. Genies, John Wiley & Sons, Inc, 1997.
- J. Ahn, J. Kang, M. kyung Cho, H. Park, W. Ko, Y. Lee, H.S. Kim, Y.H. Jung, T. Y. Jeon, H. Kim, W.H. Ryu, J. Hong, J. Kim, Selective Anionic Redox and Suppressed Structural Disorder Enabling High-Energy and Long-Life Li-Rich Layered-Oxide Cathode, *Adv. Energy Mater.* 11 (2021), <https://doi.org/10.1002/aenm.202102311>.
- Y. Lee, H. Park, M. kyung Cho, J. Ahn, W. Ko, J. Kang, Y.J. Choi, H. Kim, I. Park, W. H. Ryu, J. Hong, J. Kim, Li-Rich Mn–Mg Layered Oxide as a Novel Ni-/Co-Free Cathode, *Adv. Funct. Mater.* 32 (2022), <https://doi.org/10.1002/adfm.202204354>.
- A. Abdel-Ghany, A.M. Hashem, A. Mauger, C.M. Julien, Lithium-rich cobalt-free manganese-based layered cathode materials for li-ion batteries: Suppressing the voltage fading, *Energies.* 13 (2020) 3487, <https://doi.org/10.3390/en13133487>.
- K. Luo, M.R. Roberts, N. Niccològuerrini, N. Tapia-Ruiz, R. Hao, F. Massel, D. M. Pickup, S. Ramos, Y.-S. Liu, J. Guo, A.V. Chadwick, L.C. Duda, P.G. Bruce, Anion Redox Chemistry in the Cobalt Free 3d Transition Metal Oxide Intercalation Electrode Li[Li 0.2 Ni 0.2 Mn 0.6]O 2 Oxidation of O 2 – on charging is associated with the generation, *J. Am. Chem. Soc.* 138 (2016), <https://doi.org/10.1021/jacs.6b05111>.
- Z. Lun, B. Ouyang, D.H. Kwon, Y. Ha, E.E. Foley, T.Y. Huang, Z. Cai, H. Kim, M. Balasubramanian, Y. Sun, J. Huang, Y. Tian, H. Kim, B.D. McCloskey, W. Yang, R.J. Clément, H. Ji, G. Ceder, Cation-disordered rocksalt-type high-entropy cathodes for Li-ion batteries, *Nat. Mater.* 20 (2021) 214–221, <https://doi.org/10.1038/s41563-020-00816-0>.
- C. Cui, X. Fan, X. Zhou, J. Chen, Q. Wang, L. Ma, C. Yang, E. Hu, X.-Q. Yang, C. Wang, Structure and Interface Design Enable Stable Li-Rich Cathode, *J. Am. Chem. Soc.* 142 (2020) 8918–8927, <https://doi.org/10.1021/jacs.0c02302>.
- M. Saubanière, E. McCalla, J.M. Tarascon, M.L. Doublet, The intriguing question of anionic redox in high-energy density cathodes for Li-ion batteries, *Energy Environ. Sci.* 9 (2016) 984–991, <https://doi.org/10.1039/c5ee03048j>.
- D.H. Seo, J. Lee, A. Urban, R. Malik, S. Kang, G. Ceder, The structural and chemical origin of the oxygen redox activity in layered and cation-disordered Li-excess cathode materials, *Nat. Chem.* 8 (2016) 692–697, <https://doi.org/10.1038/nchem.2524>.
- S. Lee, W. Ko, H. Park, Y. Lee, J. Kang, J. Ahn, S. Lee, E. Sim, K. Ihm, K.Y. Park, J. Kim, Gradational anionic redox enabling high-energy P2-type Na-layered oxide cathode, *Chem. Eng. J.* 451 (2023) 138883, <https://doi.org/10.1016/j.cej.2022.138883>.
- M. Choi, H. Ahn, H. Park, Y. Lee, J. Ahn, B. Ku, J. Kim, W. Ko, J. Kang, J.K. Yoo, D.H. Seo, J. Kim, Unexpected Li displacement and suppressed phase transition enabling highly stabilized oxygen redox in P3-type Na layered oxide cathode, *J. Energy Chem.* 85 (2023) 144–153, <https://doi.org/10.1016/j.jechem.2023.06.009>.
- B. Ku, H. Ahn, S. Lee, J. Ahn, M. Choi, J. Kang, H. Park, J. Kim, A.Y. Kim, H. G. Jung, J.K. Yoo, J. Kim, Stable high-voltage operation of oxygen redox in P2-type Na-layered oxide cathode at fast discharging via enhanced kinetics, *Energy Storage Mater.* 62 (2023) 102952, <https://doi.org/10.1016/j.ensm.2023.102952>.
- J. Ahn, H. Park, W. Ko, Y. Lee, J. Kang, S. Lee, S. Lee, E. Sim, K. Ihm, J. Hong, J. K. Yoo, K. Ku, J. Kim, Occurrence of anionic redox with absence of full oxidation to Ru5+ in high-energy P2-type layered oxide cathode, *J. Energy Chem.* 84 (2023) 153–161, <https://doi.org/10.1016/j.jechem.2023.05.016>.
- M. Kalapsazova, R. Kukeva, E. Zhecheva, R. Stoyanova, Metal Substitution versus Oxygen-Storage Modifier to Regulate the Oxygen Redox Reactions in Sodium-Deficient Three-Layered Oxides, *Batteries.* 8 (2022) 56, <https://doi.org/10.3390/batteries8060056>.
- M.L. Kalapsazova, K.L. Kostov, R.R. Kukeva, E.N. Zhecheva, R.K. Stoyanova, Oxygen-Storage Materials to Stabilize the Oxygen Redox Activity of Three-Layered Sodium Transition Metal Oxides, *J. Phys. Chem. Lett.* 12 (2021) 7804–7811, <https://doi.org/10.1021/acs.jpclett.1c01982>.
- N. Guerrini, L. Jin, J.G. Lozano, K. Luo, A. Sobkowiak, K. Tsuruta, F. Massel, L.-C. Duda, M.R. Roberts, P.G. Bruce, Charging Mechanism of Li 2 MnO 3, *Chem. Mater.* 32 (2020) 3733–3740, <https://doi.org/10.1021/acs.chemmater.9b04459>.
- I. Bloom, L. Trahey, A. Abouimrane, I. Belharouk, X. Zhang, Q. Wu, W. Lu, D. P. Abraham, M. Bettge, J.W. Elam, X. Meng, A.K. Burrell, C. Ban, R. Tenent, J. Nanda, N. Dudney, Effect of interface modifications on voltage fade in 0.5Li 2 MnO 3-0.5LiNi 0.375Mn 0.375Co 0.25O 2 cathode materials, *J. Power Sources.* 249 (2014) 509–514, <https://doi.org/10.1016/j.jpowsour.2013.10.035>.
- H. Kobayashi, M. Tabuchi, M. Shikano, H. Kageyama, R. Kanno, Structure, and magnetic and electrochemical properties of layered oxides, Li₂IrO₃, *J. Mater. Chem.* 13 (2003) 957–962, <https://doi.org/10.1039/b207282c>.
- A.C.W.P. James, J.B. Goodenough, Structure and bonding in lithium ruthenate, Li₂RuO₃, *J. Solid State Chem.* 74 (1988) 287–294, [https://doi.org/10.1016/0022-4596\(88\)90357-x](https://doi.org/10.1016/0022-4596(88)90357-x).
- B. Li, R. Shao, H. Yan, L. An, B. Zhang, H. Wei, J. Ma, D. Xia, X. Han, Understanding the Stability for Li-Rich Layered Oxide Li 2 RuO 3 Cathode, *Adv. Funct. Mater.* 26 (2016) 1330–1337, <https://doi.org/10.1002/adfm.201504836>.
- S. Kang, D. Choi, H. Lee, B. Choi, Y.M. Kang, A Mechanistic Insight into the Oxygen Redox of Li-Rich Layered Cathodes and their Related Electronic/Atomic Behaviors Upon Cycling, *Adv. Mater.* 35 (2023) 2211965, <https://doi.org/10.1002/adma.202211965>.
- J. Xu, M. Sun, R. Qiao, S.E. Renfrew, L. Ma, T. Wu, S. Hwang, D. Nordlund, D. Su, K. Amine, J. Lu, B.D. McCloskey, W. Yang, W. Tong, Elucidating anionic oxygen activity in lithium-rich layered oxides, *Nat. Commun.* 9 (2018) 947, <https://doi.org/10.1038/s41467-018-03403-9>.
- N. Li, J. Wu, S. Hwang, J.K. Papp, W.H. Kan, L. Zhang, C. Zhu, B.D. McCloskey, W. Yang, W. Tong, Enabling Facile Anionic Kinetics through Cationic Redox Mediator in Li-Rich Layered Cathodes, *ACS Energy Lett.* 5 (2020) 3535–3543, <https://doi.org/10.1021/acsenenerglett.0c01880>.
- B. Li, G. Assat, P.E. Pearce, V.A. Nikitina, A. Iadecola, C. Delacourt, J.M. Tarascon, Exploring the Kinetic Limitations Causing Unusual Low-Voltage Li Reinsertion in Either Layered or Tridimensional Li₂IrO₃ Cathode Materials, *Chem. Mater.* 32 (2020) 2133–2147, <https://doi.org/10.1021/ACS.CHEMMATER.9B05362>.
- A.J. Perez, R. Beer, Z. Lin, E. Salager, P. Taberna, A.M. Abakumov, P. Simon, J. Tarascon, Proton Ion Exchange Reaction in Li 3 IrO 4: A Way to New H 3+ x IrO 4 Phases Electrochemically Active in Both Aqueous and Nonaqueous Electrolytes, *Adv. Energy Mater.* 8 (2018) 1702855, <https://doi.org/10.1002/aenm.201702855>.
- X. Cao, H. Li, Y. Qiao, M. Jia, H. Kitaura, J. Zhang, P. He, J. Cabana, H. Zhou, Structure design enables stable anionic and cationic redox chemistry in a T₂-type Li-excess layered oxide cathode, *Sci. Bull.* 67 (2022) 381–388, <https://doi.org/10.1016/j.scib.2021.11.014>.
- B. Ravel, M. Newville, ATHENA and ARTEMIS: Interactive graphical data analysis using IFEFFIT, *Phys. Scr. t* T 115 (2005) 1007–1010, <https://doi.org/10.1238/Physica.Topical.115a01007>.
- G. Kresse, J. Furthmüller, Efficiency of ab-initio total energy calculations for metals and semiconductors using a plane-wave basis set, *Comput. Mater. Sci.* 6 (1996) 15–50, [https://doi.org/10.1016/0927-0256\(96\)00008-0](https://doi.org/10.1016/0927-0256(96)00008-0).
- P.E. Blochl Projector augmented+grave method *Phys. Rev. B* 50 (n.d.) 24.
- J.P. Perdew, K. Burke, M. Ernzerhof, Generalized gradient approximation made simple, *Phys. Rev. Lett.* 77 (1996) 3865–3868, <https://doi.org/10.1103/PhysRevLett.77.3865>.
- V.I. Anisimov, F. Aryasetiawan, A.I. Lichtenstein, First-principles calculations of the electronic structure and spectra of strongly correlated systems: The LDA + U

- method, *J. Phys. Condens. Matter*. 9 (1997) 767–808, <https://doi.org/10.1088/0953-8984/9/4/002>.
- [36] A. Jain, G. Hautier, S.P. Ong, C.J. Moore, C.C. Fischer, K.A. Persson, G. Ceder, Formation enthalpies by mixing GGA and GGA + U calculations, *Phys. Rev. B - Condens. Matter Mater. Phys.* 84 (2011) 045115, <https://doi.org/10.1103/PhysRevB.84.045115>.
- [37] J. Heyd, G.E. Scuseria, M. Ernzerhof, Erratum: Hybrid functionals based on a screened Coulomb potential (*Journal of Chemical Physics* (2003) 118 (8207)), *J. Chem. Phys.* 124 (2006) 219906, <https://doi.org/10.1063/1.2204597>.
- [38] K. Momma, F. Izumi, VESTA 3 for three-dimensional visualization of crystal, volumetric and morphology data, *J. Appl. Crystallogr.* 44 (2011) 1272–1276, <https://doi.org/10.1107/S0021889811038970>.
- [39] M.D. Radin, S. Hy, M. Sina, C. Fang, H. Liu, J. Vinckeviciute, M. Zhang, M. S. Whittingham, Y.S. Meng, A. Van der Ven, Narrowing the Gap between Theoretical and Practical Capacities in Li-Ion Layered Oxide Cathode Materials, *Adv. Energy Mater.* 7 (2017) 1602888, <https://doi.org/10.1002/aenm.201602888>.
- [40] A. Van der Ven, J.C. Thomas, Q. Xu, J. Bhattacharya, Linking the electronic structure of solids to their thermodynamic and kinetic properties, *Math. Comput. Simul.* 80 (2010) 1393–1410, <https://doi.org/10.1016/j.matcom.2009.08.008>.
- [41] A. Boulineau, L. Croguennec, C. Delmas, F. Weill, Structure of Li₂MnO₃ with different degrees of defects, *Solid State Ionics*. 180 (2010) 1652–1659, <https://doi.org/10.1016/j.ssi.2009.10.020>.
- [42] R.A. House, G.J. Rees, M.A. Pérez-Osorio, J.J. Marie, E. Boivin, A.W. Robertson, A. Nag, M. Garcia-Fernandez, K.J. Zhou, P.G. Bruce, First-cycle voltage hysteresis in Li-rich 3d cathodes associated with molecular O₂ trapped in the bulk, *Nat. Energy*. 5 (2020) 777–785, <https://doi.org/10.1038/s41560-020-00697-2>.
- [43] K. Luo, M.R. Roberts, R. Hao, N. Guerrini, D.M. Pickup, Y.S. Liu, K. Edström, J. Guo, A.V. Chadwick, L.C. Duda, P.G. Bruce, Charge-compensation in 3d-transition-metal-oxide intercalation cathodes through the generation of localized electron holes on oxygen, *Nat. Chem.* 8 (2016) 684–691, <https://doi.org/10.1038/nchem.2471>.
- [44] W.E. Gent, K. Lim, Y. Liang, Q. Li, T. Barnes, S.J. Ahn, K.H. Stone, M. McIntire, J. Hong, J.H. Song, Y. Li, A. Mehta, S. Ermon, T. Tyliczszak, D. Kilcoyne, D. Vine, J. H. Park, S.K. Doo, M.F. Toney, W. Yang, D. Prendergast, W.C. Chueh, Coupling between oxygen redox and cation migration explains unusual electrochemistry in lithium-rich layered oxides, *Nat. Commun.* 8 (2017) 2091, <https://doi.org/10.1038/s41467-017-02041-x>.
- [45] R.A. House, L. Jin, U. Maitra, K. Tsuruta, J.W. Somerville, D.P. Förstermann, F. Massel, L. Duda, M.R. Roberts, P.G. Bruce, Lithium manganese oxyfluoride as a new cathode material exhibiting oxygen redox, *Energy Environ. Sci.* 11 (2018) 926–932, <https://doi.org/10.1039/c7ee03195e>.
- [46] G. Assat, A. Iadecola, D. Foix, R. Dedryvere, J.M. Tarascon, Direct quantification of anionic redox over long cycling of li-rich nmc via hard x-ray photoemission spectroscopy, *ACS Energy Lett.* 3 (2018) 2721–2728, <https://doi.org/10.1021/acsenerylett.8b01798>.
- [47] W.E. Gent, I.I. Abate, W. Yang, L.F. Nazar, W.C. Chueh, Design Rules for High-Valent Redox in Intercalation Electrodes, *Joule*. 4 (2020) 1369–1397, <https://doi.org/10.1016/j.joule.2020.05.004>.
- [48] D. Foix, M. Sathiyaa, E. McCalla, J.-M. Tarascon, D. Gonbeau, X-ray Photoemission Spectroscopy Study of Cationic and Anionic Redox Processes in High-Capacity Li-Ion Battery Layered-Oxide Electrodes, *J. Phys. Chem. c*. 120 (2016) 862–874, <https://doi.org/10.1021/acs.jpcc.5b10475>.
- [49] S.Y. Lim, H. Kim, R.A. Shakoov, Y. Jung, J.W. Choi, Electrochemical and Thermal Properties of NASICON Structured Na₃V₂(PO₄)₃ as a Sodium Rechargeable Battery Cathode: A Combined Experimental and Theoretical Study, *J. Electrochem. Soc.* 159 (2012) A1393–A1397, <https://doi.org/10.1149/2.015209jes>.
- [50] D. Eum, B. Kim, S.J. Kim, H. Park, J. Wu, S.P. Cho, G. Yoon, M.H. Lee, S.K. Jung, W. Yang, W.M. Seong, K. Ku, O. Tamwattana, S.K. Park, I. Hwang, K. Kang, Voltage decay and redox asymmetry mitigation by reversible cation migration in lithium-rich layered oxide electrodes, *Nat. Mater.* 19 (2020) 419–427, <https://doi.org/10.1038/s41563-019-0572-4>.
- [51] J. Hong, W.E. Gent, P. Xiao, K. Lim, D.H. Seo, J. Wu, P.M. Csernica, C.J. Takacs, D. Nordlund, C.J. Sun, K.H. Stone, D. Passarello, W. Yang, D. Prendergast, G. Ceder, M.F. Toney, W.C. Chueh, Metal–oxygen decoordination stabilizes anion redox in Li-rich oxides, *Nat. Mater.* 18 (2019) 256–265, <https://doi.org/10.1038/s41563-018-0276-1>.
- [52] M. Cho, S.H. Song, S. Hong, K.S. Kim, M. Avdeev, J.G. Yoo, K.T. Ko, J. Hong, J. Kim, S. Lee, H. Kim, Critical Role of Ti⁴⁺ in Stabilizing High-Voltage Redox Reactions in Li-Rich Layered Material, *Small*. 17 (2021), <https://doi.org/10.1002/sml.202100840>.
- [53] R. Santhanam, B. Rambabu, Research progress in high voltage spinel LiNi_{0.5}Mn_{1.5}O₄ material, *J. Power Sources*. 195 (2010) 5442–5451, <https://doi.org/10.1016/j.jpowsour.2010.03.067>.
- [54] G. Liang, V.K. Peterson, K.W. See, Z. Guo, W.K. Pang, Developing high-voltage spinel LiNi_{0.5}Mn_{1.5}O₄ cathodes for high-energy-density lithium-ion batteries: Current achievements and future prospects, *J. Mater. Chem. a*. 8 (2020) 15373–15398, <https://doi.org/10.1039/d0ta02812f>.
- [55] M. Sathiyaa, A.M. Abakumov, D. Foix, G. Rousse, K. Ramesha, M. Saubane, M. L. Doublet, H. Vezin, C.P. Laisa, A.S. Prakash, D. Gonbeau, G. Vantendeloo, J. M. Tarascon, Origin of voltage decay in high-capacity layered oxide electrodes, *Nat. Mater.* 14 (2015) 230–238, <https://doi.org/10.1038/nmat4137>.
- [56] Q. Li, D. Ning, D. Wong, K. An, Y. Tang, D. Zhou, G. Schuck, Z. Chen, N. Zhang, X. Liu, Improving the oxygen redox reversibility of Li-rich battery cathode materials via Coulombic repulsive interactions strategy, *Nat. Commun.* 13 (2022) 1123, <https://doi.org/10.1038/s41467-022-28793-9>.